Rapid Communications

Crystal orientation dependence of the spin-orbit coupling in InAs nanowires

T. S. Jespersen,* P. Krogstrup, A. M. Lunde, R. Tanta, T. Kanne, E. Johnson, and J. Nygård
Center for Quantum Devices and Station Q Copenhagen, Niels Bohr Institute, University of Copenhagen, Universitetsparken 5, DK-2100 Copenhagen, Denmark

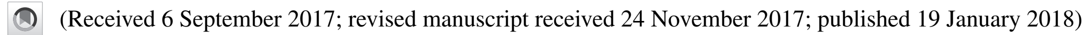

(Received 6 September 2017; revised manuscript received 24 November 2017; published 19 January 2018)

We compare the spin-orbit interaction (SOI) in InAs nanowires grown in the conventional $\langle 0001\rangle$ crystal direction and the perpendicular $\langle 01\bar{1}0\rangle$ direction. It is theoretically shown that, for individual transverse modes, the intrinsic contribution due to the bulk inversion asymmetry of the crystal vanishes for wires in the $\langle 0001\rangle$ direction but remains finite for $\langle 01\bar{1}0\rangle$. Experimental spin-orbit scattering lengths extracted from low-temperature magnetoresistance measurements of individual nanowires yields, however, comparable values in the two cases, suggesting that the intrinsic intramode spin-orbit term is not the dominant source of the SOI. We discuss the implications for the manipulation of SOI in nanowire devices.

DOI: 10.1103/PhysRevB.97.041303

Semiconductor nanowires (NWs) have constituted the material backbone of several recent breakthrough experiments in quantum transport [1–6]. In many of these cases the electron spin and its coupling to the orbital motion of the electrons, the spin-orbit interaction (SOI), has been an important ingredient. For instance, through electric dipole spin resonance, SOI allows for coherent spin control in quantum dots [5,7], and SOI is required for reaching the topologically nontrivial regime in hybrid superconductor-semiconductor nanowire devices which have recently attracted considerable attention [1,2,6,8–10]. To implement such devices in advanced nanowire networks and develop schemes for tuning or enhancing the SOI in nanowire devices, it is important to understand the origin of SOI and the relative contributions from intrinsic sources due to bulk inversion asymmetry of the crystal [11–13] and extrinsic contributions due to structural inversion asymmetry [14–16].

Previous studies of SOI in semiconductor NWs have considered structures grown either in the zinc-blende (ZB) crystal structure with the NW axis along the $\langle 111\rangle$ crystal direction or in the wurtzite (WZ) crystal structure along the $\langle 0001\rangle$ direction [17]. The intrinsic SOI due to bulk effects, however, depends strongly on the crystal directions and interestingly, as shown below, vanishes by symmetry for each individual transverse mode in wires grown in these directions. This is consistent with previous reports [1,5] of effective spin-orbit fields induced by structural asymmetries related to the interface between the NW and the supporting device substrate. Investigating SOI in wires with alternative crystal growth directions, allowing a finite contribution from intramode intrinsic SOI, can thus provide valuable information about the relative contributions to the measured SOI from extrinsic and intrinsic sources and potentially provide a route for enhancing the effective SOI. In addition, understanding the SOI in nanowires grown along alternative directions is important for the field of topological quantum information processing where branched superconductor/semiconductor nanowire geometries have been proposed as the basis for devices allowing braiding of Majorana fermions [18,19]. Investigating the link between the SOI and the nanowire crystal structure is the aim of the present Rapid Communication.

We experimentally compare the SOI in InAs WZ NWs grown in the conventional $\langle 0001\rangle$ and in the perpendicular $\langle 01\bar{1}0\rangle$ directions. Such studies have previously been complicated by the inherent difficulty of obtaining wire growth along directions different from the preferred $\langle 0001\rangle$. Here, by manipulating the wetting conditions between the semiconductor and the gold seed particle during growth, growth is effectively forced along the $\langle 01\bar{1}0\rangle$ directions [10]. Subsequently, electrical devices were fabricated in field-effect-transistor geometries, and the low-temperature phase-coherence length and spin-orbit scattering length were extracted from measurements of weak antilocalization (WAL) in the open transport regime.

Before presenting the experimental results we consider theoretically the role of crystal direction for the strength of the SOI. We choose in the following a coordinate system having the z axis along the $\langle 0001\rangle$ direction of the WZ structure. To third order in the momentum $\mathbf{k} = (k_x,k_y,k_z)$ the intrinsic SOI then becomes [11,20,21]

$$H^{\mathrm{WZ}}_{\mathrm{D,SO}} = [\lambda_0 + \lambda_c(\mathbf{k}\cdot\mathbf{c})^2 + \lambda_\perp(\mathbf{k}\times\mathbf{c})^2](\mathbf{k}\times\mathbf{c})\cdot\boldsymbol{\sigma}, \qquad (1)$$

where $\mathbf{c}$ is a unit vector along the $\langle 0001\rangle$ ($\mathbf{c}$ axis). Here $\hbar k_\nu = -i\hbar\partial_\nu$ where $\nu = x,y,z$ are the momentum operators, $\boldsymbol{\sigma} = (\sigma_x,\sigma_y,\sigma_z)$ are the Pauli matrices, and λ_0, λ_c, $\lambda_\perp$, and α are coupling constants.

For a *single* transverse mode, the dependence on the crystallographic direction becomes particularly evident. In this case, the one-dimensional SOI can be obtained by integrating out the transverse dimension [22,23]. For instance, for a NW grown along $\langle 0001\rangle$, the one-dimensional SOI vanishes ($H^{\mathrm{WZ},1D,\mathbf{c}}_{\mathrm{D,SO}} = 0$) since each term of Eq. (1) contains odd powers of transverse momentum, which integrate to zero. In contrast, for a NW grown along any direction $\mathbf{a}$ perpendicular to $\mathbf{c}$ Eq. (1) gives a nonvanishing result $H^{\mathrm{WZ},1D,\mathbf{a}}_{\mathrm{D,SO}} = k_a[\lambda_0 + \lambda_c\langle k_c^2\rangle + \lambda_\perp\langle k_b^2\rangle](\mathbf{a}\times\mathbf{c})\cdot\boldsymbol{\sigma}$. Here $\mathbf{a}$, $\mathbf{b}$,

*Author to whom correspondence should be addressed: tsand@fys.ku.dk

 ©2018 American Physical Society

and **c** are mutually perpendicular unit vectors, and $(k_a,k_b,k_c) \equiv (\mathbf{k}\cdot\mathbf{a},\mathbf{k}\cdot\mathbf{b},\mathbf{k}\cdot\mathbf{c})$.

Thus, in the single-mode limit, no intrinsic SOI is expected for NWs grown along the typical crystal directions. In contrast, if the NW is grown along the perpendicular $\langle 11\bar{2}0\rangle$ axis, nonzero contributions appear. For a multimode NW, which is often a relevant experimental limit [24,25], the above *intra*mode result remains valid, however, *inter*mode intrinsic SOI can be nonzero between, e.g., modes of opposite parity. The spin-orbit coupling measured previously for typical WZ nanowires grown in the $\langle 0001\rangle$ directions is thus a consequence of contributions of intermode intrinsic SOI and extrinsic contributions due to the inversion asymmetry of the confinement, surface accumulation layers, or the supporting substrate. Depending on the relative contributions, a stronger effective SOI may therefore be possible for NW grown in the perpendicular directions.

To enable an experimental investigation of the difference of SOI in the two directions, NWs were grown by the vapor-liquid-solid mechanism on InAs (111)B substrates by molecular beam epitaxy in a Varian Gen II solid-source system using gold nanoparticles as a catalyst. Typically, the crystal structures and symmetries are determined by the stacking sequence during growth, i.e., along $\langle 0001\rangle/\langle 111\rangle$ for WZ/ZB which are preferred as their facets perpendicular to the growth axis follow high-symmetry planes with a relatively low surface energy and therefore provide a strong thermodynamic driving force for the solidification process [26]. Alternative growth directions are, however, possible [27,28], and here we obtain NW growth along the $\langle 01\bar{1}0\rangle$ directions [29,30] by modifying the wetting conditions of the catalyst/InAs interface in the sequence illustrated in Fig. 1(a): The starting point (step 1) is an $\sim$1-μm NW stem of conventional $\langle 0001\rangle$ growth following the standard procedure (Ref. [31]). Subsequently (step 2), an $\sim$10-s pulse of gallium is introduced at a Ga flux comparable or higher than the In flux. The pulse modifies the surface energies, liquid composition, and wetting conditions at the growth region of the InAs NW crystal, forcing the Au catalyst droplet to one of the six side facets of the NW. Returning to the mode of axial InAs NW growth (step 3), the direction is then changed to be along one of the six equivalent $\langle 01\bar{1}0\rangle$ crystal orientations perpendicular to the $\langle 0001\rangle$ stem. The resulting structure has a characteristic kinked shape with a $\langle 0001\rangle$ stem and a perpendicular $\langle 01\bar{1}0\rangle$ branch. This is apparent in Fig. 1(b) which shows a side-view SEM of typical as-grown structures on the growth substrate. The initial growth of the stem is in epitaxial registry with the growth substrate, and the sixfold symmetry along the $\langle 0001\rangle$ direction of the WZ crystal leads to NW branches growing equally in all six equivalent $\langle 01\bar{1}0\rangle$ directions. This selectivity of the branch directions is clearly observed in the top-view SEM of the growth substrate in Fig. 1(c). Figure 2 presents TEM images of a typical structure. The images were acquired along the $[2\bar{1}\bar{1}0]$ zone axis, and the atomic resolution images and the selected-area diffraction of the stem and branch in panels (b) and (d) and (c) and (e), respectively, confirm the $\langle 01\bar{1}0\rangle$ direction of the branch. We note that the change in the stacking sequence away from the $\langle 0001\rangle$ direction is accompanied with a strong increase in the solid chemical potential, which can only be favorable if it can be overcome by a corresponding decrease in primarily the surface free energy. In none of the analyzed wire branches, however, has a change in the structure along $\langle 01\bar{1}0\rangle$ been observed. This shows that once the NW growth is initiated in the $\langle 01\bar{1}0\rangle$ direction, the crystal structure follows the structural phase of the stem, and even though $\langle 01\bar{1}0\rangle$ are metastable growth directions, the barrier of returning to the original and energetically favorable $\langle 0001\rangle$ direction is too large.

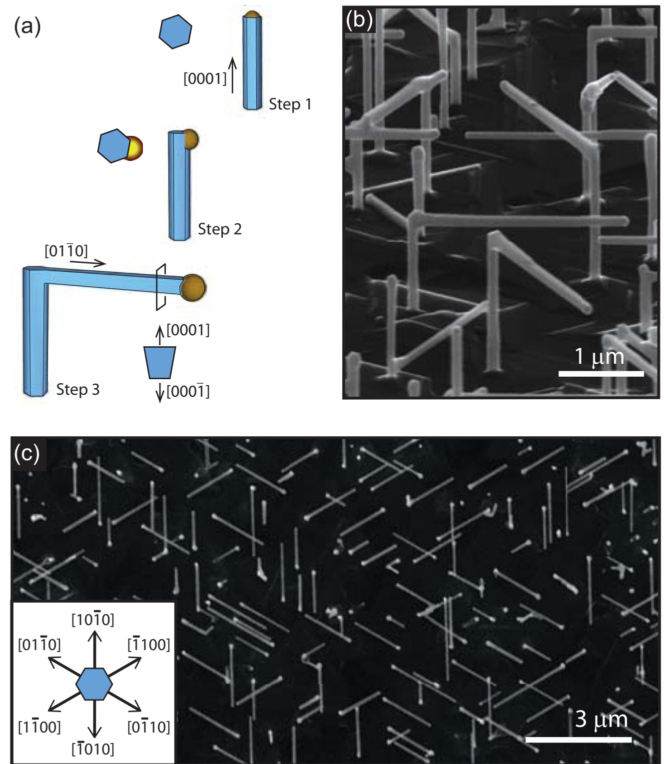

FIG. 1. (a) Schematic of the three basic main steps during the growth of the $\langle 01\bar{1}0\rangle$ nanowires. (b) Side view scanning electron micrograph (SEM) of the resulting as-grown structures, showing the characteristic kinked structure. (c) A top-view SEM image of the growth substrate. The $\langle 01\bar{1}0\rangle$ branches are parallel to the substrate and appear as lines oriented along the six equivalent directions as indicated in the inset. No preference among the six directions was observed.

To investigate the SOI of the $\langle 01\bar{1}0\rangle$ wires, electrical devices were fabricated and measured at low temperatures. The branched structures were liberated from the growth substrate by sonication in alcohol and deposited on silicon substrates with predefined metal alignment marks. By growing the $\langle 01\bar{1}0\rangle$ branch substantially longer than the $\langle 0001\rangle$ stem, the two segments of the structure can be clearly distinguished after the transfer. The device substrates are degenerately doped and used as a back gate with 500 nm of silicon oxide capping acting as the gate insulator. Wires were located by optical microscopy and titanium/gold [(5/120)-nm] electrodes were fabricated by electron-beam lithography to contact either the $\langle 01\bar{1}0\rangle$ branches or the $\langle 0001\rangle$ stem. To ensure low electrical contact resistance, the native oxide on the wires was removed by *in situ* argon-ion milling prior to metal deposition. Figure 3(a) shows an SEM image of a typical $\langle 01\bar{1}0\rangle$ device. Contact spacing was $L\sim 750$ nm, much larger than the wire diameter of $d\sim 80$ nm. The device conductance G was measured by

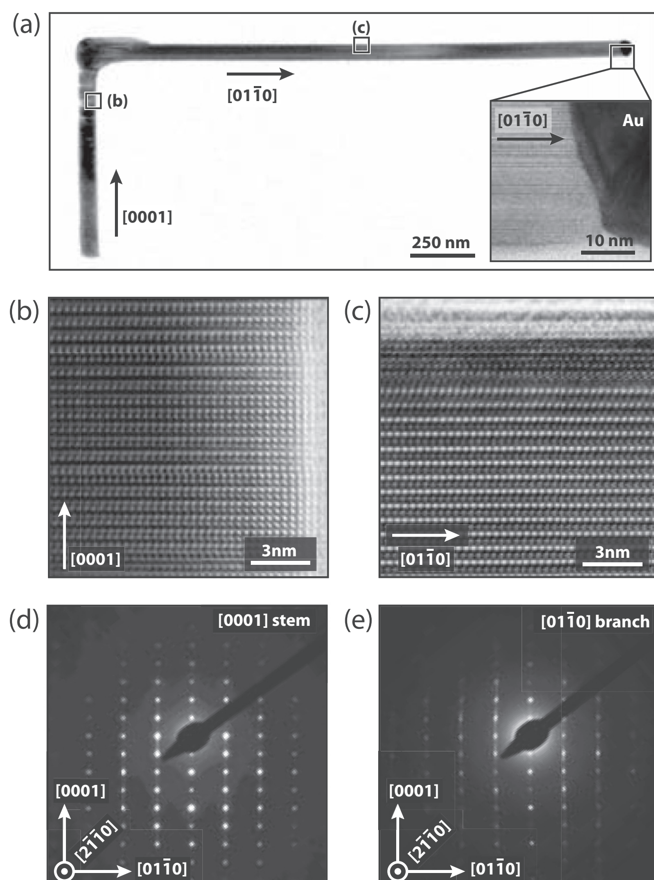

FIG. 2. (a) Transmission electron micrograph of a typical $\langle 0001\rangle/\langle 01\bar{1}0\rangle$ kinked InAs nanowire. (b) and (c) Atomic resolution TEM of the stem and branched segments as indicated in (a). (d) and (e) Selected area diffraction of the stem and branch segments, respectively. All images were acquired along the $[2\bar{1}\bar{1}0]$ zone axis. The images establish the $\langle 0001\rangle$ and $\langle 01\bar{1}0\rangle$ directions of the stem and branch, respectively, and the inset to panel (a) confirms that the $\langle 01\bar{1}0\rangle$ direction of the branch is maintained throughout the length of the nanowire.

standard lock-in techniques using a 10-μV ac excitation at a frequency of $f_{sd}^{ac} = 331$ Hz in a dilution refrigerator with a base temperature of $\sim$50 mK. In the following, we present results from measurements on two $\langle 01\bar{1}0\rangle$ devices (S1 and S2) and two $\langle 0001\rangle$ devices (S3 and S4). A typical measurement of the conductance G as a function of back-gate potential V_g is shown in Fig. 3(b) for sample S1. The $\langle 01\bar{1}0\rangle$ InAs branches behave as n-type semiconductors with increasing conductance for increasing V_g as is also the case for conventional InAs wires. The high conductance values ($\sim 7e^2/h$ at $V_g = 10$ V) indicates a low contact resistance and the occupation of several modes of the wire. This is supported by a conductance increase from $\sim$6 to $7e^2/h$ upon cooling from room temperature to 50 mK (not shown) consistent with reduced phonon scattering and opposite from the conductance freeze-out which is often observed due to suppressed thermal excitation over contact barriers. To estimate the carrier density, a cylinder-plane model is used for the back-gate capacitance using typical dimensions of the nanowire segment between the contacts and a relative dielectric constant $\epsilon = 3.9$ for the 500-nm SiO_2 separating the wire from

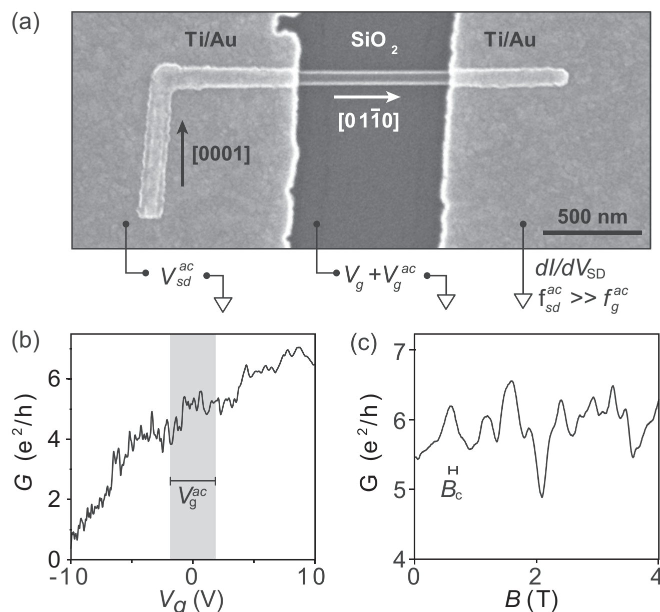

FIG. 3. (a) SEM image of an electrical device fabricated on the $\langle 01\bar{1}0\rangle$ NW branch of the $\langle 0001\rangle$ stem. (b) Conductance vs back-gate potential at $T = 50$ mK. The voltage range used for averaging the conductance fluctuations is indicated. (c) and (d) Conductance fluctuations measured as a function of magnetic field for $V_g = 0$ V.

the doped silicon back gate. This gives $C_g \sim 50$ aF, and with a threshold potential at $V_{th} \sim -11$ V [Fig. 3(b)] we find a density of 7×10^7 cm^{-1} at $V_g = 10$ V. The cross sections of the $\langle 01\bar{1}0\rangle$ wires can be approximated by a $W = 80$-nm square, and with a device length of $L = 750$ nm and the deduced density, we estimate a total of $\sim$50 populated subbands [32] at $V_g = 10$ V. In the following we analyze the low-temperature magnetotransport behavior to infer about the length scales characterizing the electron systems in the NWs.

At low temperatures the InAs nanowire can be considered as a phase-coherent quasi-one-dimensional diffusive conductor, and the conductance exhibits pronounced aperiodic reproducible fluctuations both upon varying the gate voltage [chemical potential, Fig. 3(b)] or upon varying the perpendicular magnetic field [Fig. 3(c)] due to universal conductance flucttutations (UCFs) [33,34]. The fluctuations arise due to the sensitivity of electron interference on details of the scattering and phase shifts induced by the magnetic field and can be analyzed to yield the phase-coherence length as has been studied previously for conventional InAs NWs [35,36]. After subtracting a smooth polynomial background from $G(B)$ in Fig. 3(c) the residual magnetoconductance $\delta G(B)$ is used to generate the correlation function $F_B(\delta B) = \langle \delta G(B)\delta G(B+\delta B)\rangle_B$. Here $\langle\cdot\rangle_B$ denotes an average over B. The typical scale of the fluctuations, the correlation field B_c, defined such that $F_B(B_c) = \frac{1}{2}F(0)$ then corresponds to the magnetic field needed to penetrate the typical area enclosed by phase-coherent time-reversed paths $(l_\phi d)$ by one flux quantum (h/e), i.e., $B_c(l_\phi d) = \gamma(h/e)$. The constant γ depends on the thermal length [37] $l_T = \sqrt{\hbar D/k_B T}$ which in the present case exceeds l_ϕ and [38] $\gamma = 0.42$. For samples S1 and S2 we have $B_c = 87$ and 93 mT, respectively, and $l_\phi = 250$ nm (230 nm) for S1 (S2).

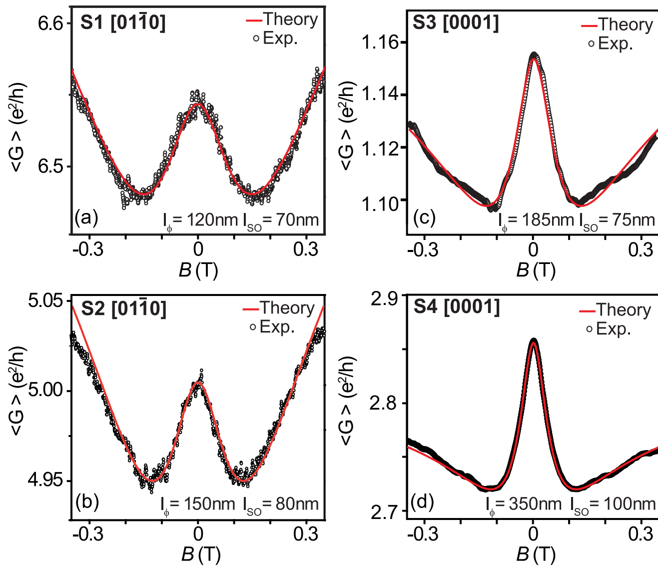

FIG. 4. (a) and (b) Average conductance $\langle G(B)\rangle_{V_g}$ for two $\langle 01\bar{1}0\rangle$ devices S1 and S2, respectively, measured at $T = 50$ mK, $V_g = 10$ V and using a 3 V $\gg V_g^c$ voltage modulation to the gate potential to average the contribution from UCF. The solid line is a fit to theory [39] with the parameters l_ϕ and l_{SO} as stated. (c) and (d) Corresponding measurement for two devices made from the stem which grows in the conventional $\langle 0001\rangle$ direction.

The strength of the spin-orbit coupling is usually investigated through measurements of weak antilocalization in the average conductance [25,35,40,41] where the contribution from UCF is removed by averaging over V_g. Previously this averaging was achieved by measuring multiple nanowires in parallel [40] or by performing two-parameter sweeps $G(V_g,B)$ and subsequent numerical averaging [25,35,41]. Here we measure the gate-averaged magnetoconductance $\langle G(B)\rangle_{V_g}$ directly by adding a low-frequency 2-Hz ac modulation of amplitude V_g^{ac} to the dc gate potential V_g. Using a $\Delta t = 10$-s averaging time on the $f_{sd}^{ac} = 331$-Hz lock-in detection of G, we effectively measure $\langle G(B)\rangle_{V_g}$. Calculating the correlation function $F_V(\delta V_g) = \langle \delta G(V_g)\delta G(V_g+\delta V_g)\rangle_{V_g}$ where $\delta G(V_g)$ is the nonaveraged gate dependence $G(V_g)$ in Fig. 3(b) after subtraction of a smooth polynomial background, we estimate the typical V_g scale of UCF fluctuations $V_g^c = 140$ mV (80 mV) as $F_V(V_g^c) = \frac{1}{2}F_V(0)$ for device S1 (S2). Setting $V_g^{ac} = 3\text{ V} \gg V_g^c$ we ensure the UCF contribution to be adequately averaged. Figure 4 shows representative measurements for the two devices. A clear peak appears at $B = 0$ T, and in analogy with similar results commonly observed in conventional $\langle 0001\rangle$ InAs NW we assign the magnetoconductance to WAL followed by a crossover to WL positive magnetoconductance beyond 0.1–0.2 T. To extract the phase-coherence length l_ϕ and the spin-orbit scattering length l_{so} from the magnetoconductance traces we used the model of Refs. [39,42]: $\Delta G(B) \propto \{[l_\phi^{-2} + \frac{1}{2}l_{so}^{-2} + (D\tau_B)^{-1}]^{-1/2} + \frac{1}{2}[l_\phi^{-2} + l_{so}^{-2} + (D\tau_B)^{-1}]^{-1/2} - \frac{1}{2}[l_\phi^{-2} + (D\tau_B)^{-1}]^{-1/2}\}$, where D is the diffusion constant and τ_B is the magnetic time such that $1/D\tau_B = (eB/h)[1 - 1/(1 + d^2e^2B^2/3\hbar^2)]$. It should be noted that the assumptions of the existing WAL theories are not strictly fulfilled for the usual measurements of WAL in InAs nanowires. For example, the theory is valid in the low-field limit for $l_m = \sqrt{\hbar/eB} \gg W$ which corresponds to $B \ll 150$ mT, however, in order to fit the data reliably the fitting interval must include the WL/WAL crossover region which usually appears at higher fields. Extracting quantitative results from such a fitting may therefore be questionable, however, the theories do reliably reproduce the expected qualitative trends [43,44] and are therefore relevant for the relative comparison of the two nanowire directions. The solid lines in Fig. 4 show the resulting fits to the data, fixing the nanowire width $d = 80$ nm and fitting in the interval from ± 0.3 T. The model describes the data excellently yielding $l_\phi = 120$ nm (150 nm) in reasonable agreement with the estimate from UCF and $l_{so} = 70$ nm (80 nm) for S1 (S2).

To compare these values with the case of conventional $\langle 0001\rangle$ NWs, devices of identical dimensions were fabricated on the stem of the kinked structures. Figures 4(c) and 4(d) show measurements of the average conductance from two such devices (S3 and S4) with densities of $\sim 3 \times 10^7$ and $\sim 6 \times 10^7$ cm^{-1}, respectively, along with fits to the WAL theory yielding spin-orbit lengths of 75 and 100 nm, respectively. Previous reports of WAL measurements on WZ $\langle 0001\rangle$ and ZB $\langle 111\rangle$ nanowires [25,35,40,41] have analyzed a range of wire diameters (60–100 nm), temperatures (0.1–8 K), and overall conductivities that are varied by electrostatic gating. For the high-conductance regime relevant for comparison to the present experiment the reported l_{so} values fall in the range of 50–150 nm, consistent with the values from the $\langle 0001\rangle$ NW. Surprisingly, however, the measurements on the perpendicular $\langle 01\bar{1}0\rangle$ nanowires where finite intraband intrinsic SOI is expected to contribute do not significantly deviate from the $\langle 0001\rangle$ references. Thus, the intraband intrinsic contribution does not add substantially to the effective SOI of nanowires, and the experiment instead points towards an extrinsic-type SOI or interband intrinsic contributions as the source of the measured SOI. This constitutes the main result of the present Rapid Communication.

Further investigations are needed to estimate their relative weight; the extrinsic SOI can be caused by the asymmetry of the confining potential at the surface which is also responsible for the surface electron accumulation layer, and this effect could potentially be isolated in structures capped in high band-gap p-doped materials. The importance of such contributions was also theoretically analyzed for ZB InAs nanowires [45]. Alternatively, the extrinsic contribution may be induced by the symmetry breaking from the supporting substrate or from the electrical field from the back gate. Insight into these contributions can be investigated by measuring the SOI in freely suspended wires and the dependence on the direction of the electrical field in multigate devices [44]. The results suggest that the crystal orientation dependence of SOI does not impose additional constraints on the design of complex branched NW network devices, such as those proposed for the braiding of Majorana fermions [18,19].

We acknowledge E. Rashba and C. M. Marcus for useful discussions and L. Zhang, Center for Electron Nanoscopy, Technical University of Denmark for TEM support. The work

was financially supported by the Villum Foundation (T.S.J.), Innovation Fund Denmark, QuBiz (T.S.J. and J.N.), Microsoft Research (P.K.), University of Copenhagen Excellence Program, Biosynergy (R.T.. and J.N.), and the Carlsberg Foundation (A.M.L.). The Center for Quantum Devices is funded by the Danish National Research Foundation.

[1] V. Mourik, K. Zuo, S. M. Frolov, S. R. Plissard, E. P. A. M. Bakkers, and L. P. Kouwenhoven, Science **336**, 1003 (2012).

[2] A. Das, Y. Ronen, Y. Most, Y. Oreg, M. Heiblum, and H. Shtrikman, Nat. Phys. **8**, 887 (2012).

[3] L. Hofstetter, S. Csonka, J. Nygård, and C. Schoenenberger, Nature (London) **461**, 960 (2009).

[4] J. van Dam, Y. Nazarov, E. Bakkers, S. De Franceschi, and L. Kouwenhoven, Nature (London) **442**, 667 (2006).

[5] S. Nadj-Perge, S. M. Frolov, E. P. A. M. Bakkers, and L. P. Kouwenhoven, Nature (London) **468**, 1084 (2010).

[6] M. T. Deng, C. L. Yu, G. Y. Huang, M. Larsson, P. Caroff, and H. Q. Xu, Nano Lett. **12**, 6414 (2012).

[7] M. D. Schroer, K. D. Petersson, M. Jung, and J. R. Petta, Phys. Rev. Lett. **107**, 176811 (2011).

[8] Y. Oreg, G. Refael, and F. von Oppen, Phys. Rev. Lett. **105**, 177002 (2010).

[9] R. M. Lutchyn, J. D. Sau, and S. Das Sarma, Phys. Rev. Lett. **105**, 077001 (2010).

[10] P. Krogstrup, N. L. B. Ziino, W. Chang, S. M. Albrecht, M. H. Madsen, E. Johnson, J. Nygård, C. M. Marcus, and T. S. Jespersen, Nature Mater. **14**, 400 (2015).

[11] G. Dresselhaus, Phys. Rev. **100**, 580 (1955).

[12] E. I. Rashba, Sov. Phys. Solid State **1**, 368 (1959).

[13] E. I. Rashba and V. I. Sheka, Fiz. Tverd. Tela: Collected Papers **2**, 162 (1959).

[14] Y. A. Bychkov and E. I. Rashba, J. Phys. C: Solid State Phys. **17**, 6039 (1984).

[15] G. Bihlmayer, O. Rader, and R. Winkler, New J. Phys. **17**, 050202 (2015).

[16] J. Fabian, A. Matos-Abiague, C. Ertler, P. Stano, and I. Zutic, Acta Phys. Slovaca **57**, 565 (2007).

[17] Here the four indices are the conventional Miller-Bravais indices of the hexagonal structure.

[18] J. Alicea, Y. Oreg, G. Refael, F. von Oppen, and M. P. A. Fisher, Nat. Phys. **7**, 412 (2011).

[19] T. Hyart, B. van Heck, I. C. Fulga, M. Burrello, A. R. Akhmerov, and C. W. J. Beenakker, Phys. Rev. B **88**, 035121 (2013).

[20] L. C. L. Y. Voon, M. Willatzen, M. Cardona, and N. E. Christensen, Phys. Rev. B **53**, 10703 (1996).

[21] I. Zorkani and E. Kartheuser, Phys. Rev. B **53**, 1871 (1996).

[22] B. A. Bernevig and S.-C. Zhang, Phys. Rev. Lett. **95**, 016801 (2005).

[23] C. H. L. Quay, T. L. Hughes, J. A. Sulpizio, L. N. Pfeiffer, K. W. Baldwin, K. W. West, D. Goldhaber-Gordon, and R. de Picciotto, Nat. Phys. **6**, 336 (2010).

[24] X. Zhou, S. A. Dayeh, D. Aplin, D. Wang, and E. T. Yu, J. Vac. Sci. Technol. B **24**, 2036 (2006).

[25] P. Roulleau, T. Choi, S. Riedi, T. Heinzel, I. Shorubalko, T. Ihn, and K. Ensslin, Phys. Rev. B **81**, 155449 (2010).

[26] P. Krogstrup, H. I. Jørgensen, E. Johnson, M. H. Madsen, C. B. Sørensen, A. Fontcuberta i Morral, M. Aagesen, J. Nygård, and F. Glas, J. Phys. D: Appl. Phys. **46**, 313001 (2013).

[27] B. Tian, P. Xie, T. J. Kempa, D. C. Bell, and C. M. Lieber, Nat. Nanotechnol. **4**, 824 (2009).

[28] J. Wang, S. Plissard, M. Hocevar, T. T. T. Vu, T. Zehender, G. G. W. Immink, M. A. Verheijen, J. Haverkort, and E. P. A. M. Bakkers, Appl. Phys. Lett. **100**, 053107 (2012).

[29] K. A. Dick, K. Deppert, L. S. Karlsson, W. Seifert, L. R. Wallenberg, and L. Samuelson, Nano Lett. **6**, 2842 (2006).

[30] Z.-A. Li, C. Möller, V. Migunov, M. Spasova, M. Farle, A. Lysov, C. Gutsche, I. Regolin, W. Prost, F.-J. Tegude *et al.*, J. Appl. Phys. **109**, 114320 (2011).

[31] P. Krogstrup, J. Yamasaki, C. B. Sørensen, E. Johnson, J. B. Wagner, R. Pennington, M. Aagesen, N. Tanaka, and J. Nygård, Nano Lett. **9**, 3689 (2009).

[32] We have also tested other cross-sectional geometries, and we find between ∼40 and 55 modes at $V_g = 10$ V for cross sections that are square, rectangular with slightly different side lengths, solid cylinder, and a circular model where the electrons only occupy the wire surface. In all cases the multimode regime holds.

[33] P. A. Lee, A. D. Stone, and H. Fukuyama, Phys. Rev. B **35**, 1039 (1987).

[34] P. A. Lee and A. D. Stone, Phys. Rev. Lett. **55**, 1622 (1985).

[35] S. E. Hernández, M. Akabori, K. Sladek, C. Volk, S. Alagha, H. Hardtdegen, M. G. Pala, N. Demarina, D. Grützmacher, and T. Schäpers, Phys. Rev. B **82**, 235303 (2010).

[36] C. Blömers, M. I. Lepsa, M. Luysberg, D. Gruetzmacher, H. Lueth, and T. Schäpers, Nano Lett. **11**, 3550 (2011).

[37] The thermal length $l_T = \sqrt{\hbar D/k_B T}$ is determined as outlined in Ref. [38]. At $V_g = 10$ V the high-temperature conductance of the device is $G_{\mathrm{High}\,T} \sim 6e^2/h$, and the value of the diffusion constant $D \sim 0.1$ m^2/s is found from the relation $G_{\mathrm{High}\,T} = (me^2/\pi\hbar^2)(d/L)D$. From this we find $l_T \sim 4$ μm which significantly exceeds l_ϕ, and thus we take $\gamma = 0.42$ appropriate for this limit.

[38] C. W. J. Beenakker and H. van Houten, Solid State Phys. **44**, 1 (1991).

[39] S. Kettemann, Phys. Rev. Lett. **98**, 176808 (2007).

[40] A. E. Hansen, M. T. Björk, C. Fasth, C. Thelander, and L. Samuelson, Phys. Rev. B **71**, 205328 (2005).

[41] S. Dhara, H. S. Solanki, V. Singh, A. Narayanan, P. Chaudhari, M. Gokhale, A. Bhattacharya, and M. M. Deshmukh, Phys. Rev. B **79**, 121311 (2009).

[42] A. Wirthmann, Y. S. Gui, C. Zehnder, D. Heitmann, C. M. Hu, and S. Kettemann, Physica E **34**, 493 (2006).

[43] D. Liang and X. P. A. Gao, Nano Lett. **12**, 3263 (2012).

[44] Z. Scherübl, G. Fülöp, M. H. Madsen, J. Nygård, and S. Csonka, Phys. Rev. B **94**, 035444 (2016).

[45] M. Kammermeier, P. Wenk, J. Schliemann, S. Heedt, and T. Schäpers, Phys. Rev. B **93**, 205306 (2016).